EDGE ARTICLE

Check for updates

A nickel-based metal–organic framework as a new cathode for chloride ion batteries with superior cycling stability†

Qing Yin,[a] Zhihao Song,[a] Shuhan Yang,[a] Gang-Ding Wang,[b] Yanwei Sui, [ID] *[a] Jiqiu Qi, [ID] [a] Danyang Zhao, [ID] [a] Lei Hou [ID] *[b] and Yong-Zhi Li [ID] *[a]

Chloride ion batteries (CIBs) have drawn growing attention as attractive candidates for large-scale energy storage technology because of their high theoretical energy densities (2500 W h L^{-1}), dendrite-free characteristics and abundance of chloride-containing materials available worldwide. However, the further development of CIBs is greatly limited by sluggish Cl$^-$ diffusion and distinct structural variation of cathode materials, resulting in severe decayed capacity and inferior rate performance. Metal–organic framework (MOF) materials possess regular pores/channels and flexible structural designability to accommodate charge carrier ions, but the application of MOFs in anion-type batteries has not been reported. Here, we demonstrate the first example of Ni(dpip) with two different opening sizes of tubular channels serving as the cathode for high performance CIBs. The Ni-based MOF exhibited a stable reversible capacity of 155 mA h g^{-1} with an admirable low capacity decay of 0.026% per cycle over 500 cycles and superior kinetics with a 10^{-10} cm^2 s^{-1} average diffusion coefficient for chloride ions as well. The high performance of the Ni(dpip) cathode results from the synergetic redox couples of Ni metal nodes and N-ligands, the unique double-channel structure for reversible Cl-storage, and the low chloride diffusion energy barrier. This work switches on the new application of MOF-based materials as cathodes for CIBs.

Introduction

Recently, anion-shuttle batteries (ASBs) with anions as charge carriers, including halogen anions (F$^-$, Cl$^-$ and Br$^-$) and complex anions (PF$_6^-$, TFSI$^-$, AlCl$_4^-$, ClO$_4^-$, NO$_3^-$ and [ZnCl$_4$]$_2^-$), have played an important role in developing new rechargeable battery chemistries, because of their large theoretical energy density, environmental friendliness and cost competitiveness.[1–4] Specifically, chloride-ion batteries (CIBs) possess the advantages of a theoretical volumetric energy density of 2500 W h L^{-1} and the worldwide availability of chloride-containing precursor materials, which all facilitate the CIB as a representative electrochemical system for sustainable grid-scale energy storage.[5–9] Up to now, several studies have been devoted to exploring new cathode materials for Cl$^-$ storage. For instance, conversion-type metal chlorides (CoCl$_2$ or

FeCl$_3$)[10]/oxychlorides (BiOCl,[11] FeOCl[12] and VOCl[13]) are inexpensive and have large value in theoretical capacity. But the large volumetric change during chlorination/de-chlorination triggers severe pulverization and collapse of these materials which lead to the serious irreversibility of such CIBs.[14] Afterwards, intercalation-type layered double hydroxides (LDHs) were reported as promising cathodes for CIBs due to their unique topological characteristics and high redox activity.[15–17] However, the intrinsic poor conductivity and limited surface area of LDH powder materials induce severe decay of initial capacity and sluggish Cl$^-$ diffusion problems for LDH-based CIBs.[18] Thus, the intense exploration of desirable cathodes with superior kinetics and capacity retention stability for reversible Cl$^-$ storage holds great significance for the development of CIBs.

Metal–organic frameworks (MOFs), consisting of metal nodes (ions or clusters) and organic linkers, have attracted tremendous attention in energy storage and conversion.[19,20] Compared with conventional inorganic materials, the intrinsic well-defined crystalline frameworks of MOFs ensure their outstanding structural stability and uniformly distributed electroactive sites.[21–23] Moreover, MOFs with permanent porosity and a prominent specific surface area also exhibit rapid electrolyte penetration and enhanced ion diffusion transport. Therefore, MOF materials have obtained great success in cation-

[a]Jiangsu Province Engineering Laboratory of High Efficient Energy Storage Technology and Equipments, School of Materials and Physics, China University of Mining and Technology, Xuzhou 221116, P. R. China. E-mail: Lyz2021@cumt.edu.cn; wyds123456@outlook.com

[b]Key Laboratory of Synthetic and Natural Functional Molecule of the Ministry of Education, College of Chemistry & Materials Science, Northwest University, Xi'an 710069, P. R. China. E-mail: lhou2009@nwu.edu.cn

† Electronic supplementary information (ESI) available: Crystallography data and additional figures. See DOI: https://doi.org/10.1039/d3sc01497e

based batteries such as Li–S batteries,[24–27] sodium-ion batteries (SIBs)[28,29] and potassium-ion batteries (PIBs),[30–32] benefiting from their versatile structures and metal–ligand coordination chemistry properties. Nevertheless, the feasibility of MOF-based electrodes in ASBs has not been reported yet. Considering the above discussion, selection of compatible organic ligands, designing MOFs with advantageous frameworks to accommodate anions, and investigating the anionic energy storage mechanism of MOF materials offer great promise for the crucial development of ASBs.

Here, a novel nickel-based MOF ([Ni(dpip)]), which has an open porous framework with electrochemically active metal centers in four directions, was studied as a cathode for CIBs. The Ni(dpip) cathode shows a remarkable Cl$^-$ storage performance: a stable reversible capacity of $\approx$155 mA h g^{-1} over 500 cycles with an extremely low capacity decay of 0.026% per cycle at a current density of 150 mA g^{-1}. This is the first example of a new cathode for high performance ASBs made entirely from neat MOFs as active materials. Ni(dpip) possesses uniform mesopores and double one-dimensional (1D) tubular channels with different opening sizes, which provide high exposure of active sites and are beneficial for feasible Cl$^-$ diffusion simultaneously. Furthermore, the reversible chemical state changes in Ni^{2+}/Ni^{3+} and N^0/N^{1+} couples during the charge/discharge process confirmed the energy storage mechanism of the synergetic contributions from both metal ions and organic ligands for the MOF-based CIBs. This study opens up an avenue for application of MOF electrode materials and discovers a new family of attractive cathodes for anion-type rechargeable batteries.

Results and discussion

The chemical formula of Ni-MOF can be described as [Ni(dpip)], which is confirmed by single-crystal X-ray diffraction and thermogravimetric analysis (TGA).[33] The Ni-MOF crystallizes in a tetragonal $I\bar{4}c2$ space group, consisting of double tubular channels with different open sizes (9.5 Å and 6.6 Å) and surface groups, including pyridine rings and carboxy O atoms, which provides a favourable environment for Cl$^-$ storage and transmission (Fig. 1a). TGA analysis revealed a high thermostable temperature of 400 °C (Fig. S1†). The PXRD pattern of the synthesized samples is in good agreement with that simulated from the corresponding crystal structure, proving the good phase purity of Ni-MOF (Fig. 1b).

The N$_2$ adsorption test at 77 K confirms the permanent porosity of the activated Ni-MOF. As shown in Fig. 1c, the saturated N$_2$ uptake is 376 cm^3 g^{-1}, and the fitted BET surface area and pore volume are 1011.7 m^2 g^{-1} and 0.54 cm^3 g^{-1}, respectively. The morphology and microstructure of the [Ni(dpip)] sample were investigated by scanning electron microscopy (SEM) and transmission electron microscopy (TEM). Both images indicate that the Ni-MOF possesses the regular blocky-shape morphology and elemental mapping further shows that C, N, O, and Ni elements are homogeneously distributed in the sample (Fig. 1d and 2a, see the digital photograph in Fig. S2†). Subsequently, the surface chemical valence state of Ni-MOF was further determined by X-ray photoelectron spectroscopy (XPS). The survey spectrum (Fig. S3†) shows the existence of C, N, O, and Ni elements in the MOF. Fig. 2b (left) presents the high-resolution XPS spectrum of Ni 2p and the binding energies at 855.8 and 873.4 eV are identified for Ni^{2+}.[34] For N 1s spectra shown in Fig. 2b (middle), the fitting peak at 399.3 was reported for pyridinic-N species in the dpip ligand.[35] In addition, the O1s spectra of Ni-MOF are composed of peaks at binding energies 531.3 eV (O1), 530.8 eV (O2) and 532.4 (O3), showing the presence of metal–oxygen (M–O) bonds, O–H bonds of H$_2$O in Ni-MOF and O–O bonds from adsorbed molecular oxygen, respectively.

After an activation process by chlorination (pre-charge), the typical sloping profile of the Ni(dpip) cathode with an initial high discharge capacity of 178.1 (83.5% of the theoretical discharge capacity based on the asymmetric unit molar formula) mA h g^{-1} was obtained as shown in Fig. 3a and S4.† Meanwhile, the curves of NiSO$_4$ and the pure 4,6-di(pyridin-4-yl) isophthalic acid ligand both display a similar shape to Ni(dpip) but a rather low capacity of 16.8 mA h g^{-1} and 52.9 mA h g^{-1}. Moreover, as shown in Fig. 3b, the Ni(dpip) cathode delivers

Fig. 1 (a) Three-dimensional (3D) framework of Ni(dpip); (b) PXRD pattern Ni(dpip) (inset: detailed display of channels along the c-axis); (c) N$_2$ sorption isotherm of Ni(dpip); (d) SEM image of Ni(dpip).
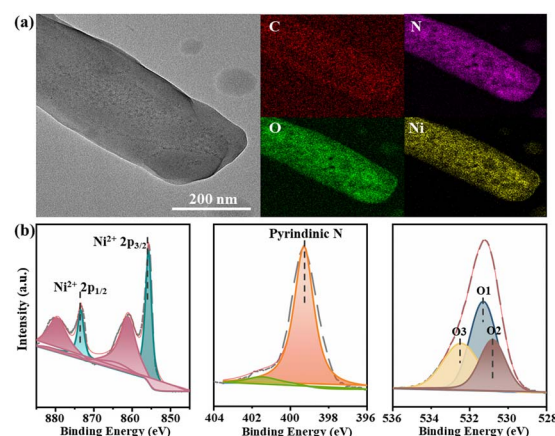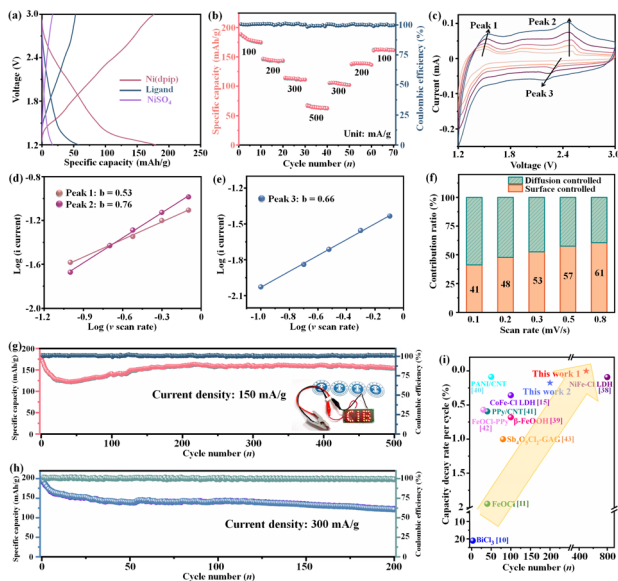

Fig. 2 (a) TEM image with EDS mapping of Ni(dpip); (b) Ni, N and O XPS spectra of Ni(dpip).

Fig. 3 (a) Charge/discharge curves of the Ni(dpip) cathode, NiSO$_4$ and the dpip ligand; (b) rate performance of the Ni(dpip) cathode; (c) CV curves of a Li‖Ni(dpip) CIB at various scan rates of 0.1, 0.2, 0.3, 0.5 and 0.8 mV s^{-1}; calculation of b values from the relationship between log(i) and log(v) of (d) peak 1, peak 2, and (e) peak 3; (f) the percent of pseudocapacitive contribution at different scan rates. Cycling performances of the Ni(dpip) cathode at current densities of (g) 150 mA g^{-1} and (h) 300 mA g^{-1}; (i) Comparison study of electrochemical performance between the Li‖Ni(dpip) CIB in this work and other reported CIBs.

$$i = k_1v + k_2v^{1/2}$$

As shown in Fig. 3f, the surface controlled contributions for the Cl$^-$ storage are 41%, 48%, 53%, 57% and 61% at corresponding scan rates of 0.1, 0.2, 0.3, 0.5 and 0.8 mV s^{-1} (Fig. S5†).

When operated at a current density of 150 mA g^{-1}, the Ni(dpip) cathode is capable of delivering a stabilized capacity of $\approx$155 mA h g^{-1} after 500 cycles with a steady coulombic efficiency of $\approx$100% as shown in Fig. 3g, demonstrating outstanding long-term cycling performance. Furthermore, the selected charge and discharge curves of the Li/BPy14Cl-PC/Ni(dpip) CIB indicate the superior voltage stability during the cycling (Fig. S6†). Since it is unavoidable that the discharge product of LiCl on the surface of the lithium anode may dissolve in the CIB during long cycling, even given its low solubility in PC solvent, the interference arising from Li-accommodate in the Ni(dpip) cathode cannot be ignored. As shown in Fig. S7,† even when using the LiPF$_6$-EC-DMC-PC electrolyte, Ni(dpip) could only deliver just 33 mA h g^{-1} discharge capacity with the same operating parameters of CIBs. Additionally, based on the lithium ion transport, the charge/discharge profiles of the Li/LiPF$_6$-EC-DMC-PC/Ni(dpip) cell shown in Fig. S8† are completely different from those of the Li/BPy14Cl-PC/Ni(dpip) CIB and display an obvious discharge plateau at 1.8 V and charge plateau at around 2.2 V. In order to confirm the advantages of the unique double 1D diffusion channel structure of Ni(dpip), electrochemical performances of NiSO$_4$ and the pure 4,6-di(pyridin-4-yl) isophthalic acid ligand were also investigated in CIB systems at a current density of 150 mA g^{-1}. The result shows that metal–salt NiSO$_4$ presented almost no capacity for Cl$^-$ storage (Fig. S9†). However, the 4,6-di(pyridin-4-yl) isophthalic acid ligand displayed a relatively better discharge capacity of 56 mA h g^{-1} (Fig. S10†), which was probably due to the hetero-atoms in the pyridine group.

Most significantly, the Ni(dpip) cathode exhibits a negligible capacity decay of 0.026% per cycle, which is the best level among those of all previously reported cathodes for CIBs. Additionally, the Ni(dpip) cathode could also maintain a reversible discharge capacity of 121.6 mA h g^{-1} at a higher current density of 300 mA g^{-1}, with a good capacity decay of 0.17% per cycle over 200 charge/discharge reactions (Fig. 3h). It should be admitted that the discharge platform of CIBs is not as good as that of some cation-based batteries at present. However, such CIBs still remain attractive, because chloride materials are more widely available for sustainable utilization or low cost and another extraordinary characteristic is that they are metal dendrite-free, which makes CIB systems more secure for practical application (Fig. S11†). From the comparison study shown in Fig. 3i and Table S1†,[10,11,15,38–43] the Ni-MOF material shows great potential in terms of the satisfactory capacity and excellent reversibility of CIBs.

The *ex situ* XRD patterns of the Ni(dpip) cathode at various electrochemical states are shown in Fig. S12.† It is worth noting that during the whole cycling process, no new diffraction peak is observed for the cathode, except that the crystallinity of Ni(dpip) becomes weakened at high voltage, which probably

discharge capacities of 175.2, 143.9, 111.3 and 62.6 mA h g^{-1} at various rate capacities tested from 100 to 500 mA g^{-1}. When the current densities were set back to lower densities gradually, the capacities also returned to 102.1, 136.3 and 161.2 mA h g^{-1} respectively, indicating the robust reversible redox behavior. The desirable rate performance can be ascribed to the open porous frameworks and organic structural flexibility of Ni-MOF which will be discussed in the following mechanism section.

The electrochemical dynamics of Cl$^-$ storage for Ni(dpip) was explored using CV measurements at different scan rates ranging from 0.1 to 0.8 mV s^{-1} (Fig. 3c). Generally, the relationship between peak current (i) and the scan rate (v) obeys a power-law as follows:

$$i = av^b$$

where a b value of 1.0 refers to a surface capacitive-controlled behavior while a b value of 0.5 indicates a semi-infinite linear diffusion dominated charge storage process.[36] The calculated b-values of the Ni(dpip) cathode are 0.53, 0.76 and 0.66 (Fig. 3d and e), which are determined using the slopes of the log(v) *versus* log(i) plot from three redox peaks (peak 1, peak 2 and peak 3). The results reveal that diffusion and surface controlled energy storage mechanisms coexist for the Li‖Ni(dpip) CIB. The contribution fractions from diffusion-control and capacitive-control are quantitatively evaluated using the values of k_1 and k_2 in the following equation:[37]

results from successive insertion of chloride ions. The *ex situ* XPS technique was performed to probe the Cl-storage mechanism during the charge/discharge process in the Ni(dpip)-based CIB. The enlarged views of Ni $2p_{3/2}$ core regions at different voltage stages are shown in Fig. 4a and b, displaying the reversible evolution between Ni^{2+} and Ni^{3+}. During the charge reaction, the peak intensity at a binding energy of 856.8 eV, which is identified for Ni^{3+}, increases from the initial 1.2 V electrode sample. When the Ni(dpip) cathode charges to 2.5 V, the integration of peak areas for Ni^{3+}/Ni^{2+} changes from 0 to 2.55 (Fig. 4e), as a result of Cl^- intercalation. At the end of charging (the sample at 3.0 V), the characteristic peak of Ni^{2+} at 855.6 eV disappears completely, indicating that all the Ni^{2+} in the original Ni-MOF are oxidized to Ni^{3+}. Upon the following discharge, the intensity of the Ni^{2+} peak gradually recovers and the ratio of Ni^{3+}/Ni^{2+} peak integrals decreases from 2.08 at 2.3 V to 0.37 at 1.4 V. When the discharge process is completely finished, the oxidized coordination center of Ni^{3+}(dpip) almost returned to its initial state of Ni^{2+} before cycling, implying the highly reversibility of the Ni^{2+}/Ni^{3+} couple in the Ni(dpip) cathode. The oxidation state variations of Ni^{2+}/Ni^{3+} during cycling were further confirmed through *ex situ* X-ray absorption near-edge structure (XANES) spectroscopy, in which the threshold energy position of K-edge XANES spectra of transition metals is very sensitive to their valence states. As depicted in Fig. S13,† the K-edge XANES spectra for the Ni node exhibit a typically rigid edge shift towards higher energy continuously with the increase of voltage states, verifying the oxidation of Ni^{2+}

to Ni^{3+} due to the insertion of chloride ions *via* electrostatic force.

Considering that the mass ratio of metal nodes is relatively low in relation to the entire Ni-MOF molecule, the oxidation states of pyridine N atoms were also investigated during the electrochemical reaction. N 1s XPS spectra of the Ni(dpip) electrode at different states in Cl-insertion (1.2, 1.8, 2.2, 2.5 and 3.0 V) and Cl-deinsertion (3.0, 2.3, 1.7, 1.4 and 1.2 V) processes are presented in Fig. 4c and d. All the observed peaks of high-resolution N 1s can be deconvoluted into two characteristic peaks at binding energies of 399.15 and 402.09 eV, which are assigned to neutral N^0 (blue area) and oxidized N^+ (orange area) respectively.[44] As presented in Fig. 4c, the N^+ signal increases at the expense of the N^0 signal, and the N^+/N^0 ratio also increases from 0.99 to 7.31 as shown in Fig. 4f, demonstrating that the increasing Cl^- insertion extent results in the significant oxidation of N atoms with an increase in voltage. When discharged to 2.3 V, the N^+/N^0 ratio decreases dramatically to 2.05, from which it could be concluded that the transformation between N^+ and N^0 tends to occur at higher potential. Upon discharging, an obvious recovery is also observed for the intensity of N^0 and the ratio of the N^+/N^0 peak integrals ($N^+/N^0 = 1.09$) at 1.2 V almost fully returns to its initial value before cycling, which attributes to reduction of the N element in the Ni(dpip) cathode for charge balance accompanied by the de-insertion of Cl^-. To display directly the reversible migration of chloride ions between the two electrodes, XPS spectra of the Cl 2p region at different voltage states are shown in Fig. 4g. During the charging process,
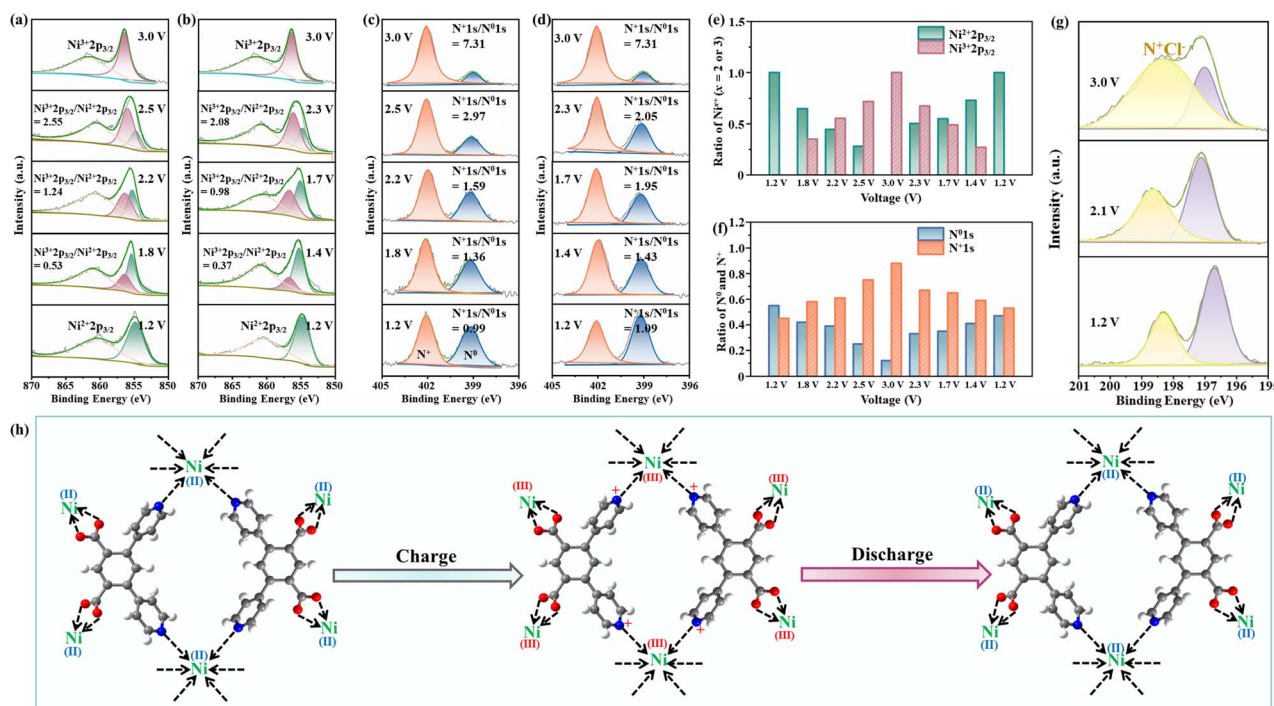

Fig. 4 *Ex situ* XPS spectra of the Ni $2p_{3/2}$ region at various voltage states in (a) charge and (b) discharge processes; *ex situ* XPS spectra/of the N 1s region at various voltage states in (c) charge and (d) discharge processes; the relative ratio of peak integrated areas for (e) Ni^{2+} $2p_{3/2}/Ni^{3+}$ $2p_{3/2}$ and (f) N^0 1s/N^+ 1s; (g) XPS spectra of the Cl 2p region at various voltage states; (h) the electrochemical reaction of the Li/Bpy14Cl-PC/Ni(dpip) CIB system.

the ratio of the intermediate anionic chloride species involved in the charge transfer interactions between the pyridine N in Ni(dpip) and the chloride ion increases at the expense of the ionic chloride species.[45] All the aforementioned results suggest that the high-capacity Cl^- ion storage performance of this unique Ni-MOF electrode is ascribed to synergetic contributions of N^0/N^+ and Ni^{2+}/Ni^{3+} reversible redox couples (Fig. 4h). For the Li anode, the XRD pattern (Fig. S14†) displays the diffractions ascribed to the LiCl phase after being fully discharged, indicating that the chloride ions transferred to the Li anode to form LiCl on the surface. Meanwhile, as shown in Fig. S15,† no extra peak was observed in the XRD patterns of the Ni(dpip) cathode after the 200th cycle, suggesting no significant phase evolution during the electrochemical process.

To further verify the pivotal role of the two different 1D tubular channels in the Ni(dpip) electrode in terms of excellent chloride storage performance, the Cl^- ion diffusion in Ni(dpip) was simulated using the climbing image nudged elastic band (CI$^-$NEB) method. One of the diffusion pathways of Cl^- in the Ni(dpip) side channel is shown in Fig. 5a, which shows that a large opening size of 9.5 Å provides adequate space for Cl^- iona to migrate. The chloride migration energy barrier in such large scale molecules is just 0.67 eV (Fig. 5b). Besides the conventionally capacious channel ionic diffusion behavior, Cl^- ionic diffusion in the central channel of Ni(dpip) with an opening size of 6.6 Å was also considered (Fig. 5c). As depicted in Fig. 5d, the migration energy barrier of this channel for Cl^- diffusion is estimated to be ≈0.9 eV, which is a little higher than that of side channel migration but still feasible for Cl^- diffusion. Considering that the side channel is formed by the ligand pyridine ring connected with Ni nodes compared to the central one, density functional theory (DFT) calculations also well supported that the lower migration energy barrier of the side channel is beneficial for the charge exchange behavior between ligand-N and Cl^-.
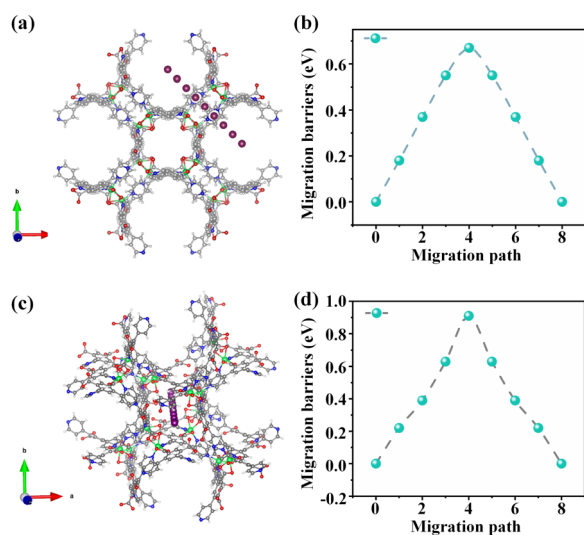
For better illustrating the unique structural advantages of Ni(dpip), the electrochemical performances of three different MOF materials were evaluated in CIB systems subsequently. First, HKUST-1 is a classical 3D framework formed by the connection of paddle wheel type $[Cu_2(OOC)_4]$ SBUs and btc ligands, as shown in Fig. S16a,† which possesses an accessible porosity of 50% with a pore size of 1 nm. Despite the high porosity and large aperture, the HKUST-1 cathode displays negligible Cl-storage capacity (Fig. S16b†) due to the Cu nodes and carboxylic acid-type ligand without N hetero-atoms. For the next reference sample shown in Fig. S17a,† the adjacent Ni(II) ions in $[Ni_3(btc)_2(bipy)_3(H_2O)_2]$ are connected by btc to form a coplanar layer, and the layers are supported by bipy to form a 3D framework with a narrow oblong channel of ca. 2.0×7.9 Å^2. As depicted in Fig. S17b,† the $[Ni_3(btc)_2(bipy)_3(H_2O)_2]$ cathode shows a maximum discharge capacity of 53.4 mA h g^{-1} but a poor capacity retention of 41.9% after 100 cycles. In contrast, $[Ni\text{-}(4Pyc)_2 \cdot DMF]$ (Fig. S18a†), which has square channels with an effective size of about 7.0×7.0 Å^2 along the a-axis by connecting isolated Ni(II) ions with 4-pyridyl carboxylic acid ligands, shows a reasonable improved maximum discharge capacity of 107.9 mA h g^{-1} with a moderate capacity retention of 67.4% (Fig. S18b†).

The galvanostatic intermittent titration technique (GITT) was applied as an efficient method to calculate chemical diffusion coefficients. (The time versus the voltage curve for a single titration is shown in the ESI, Fig. S19†.) As shown in Fig. 6a, the average Cl^- diffusion coefficients of Ni(dpip) are between 10^{-11} and 10^{-9} cm^2 s^{-1} during the charge/discharge process, which demonstrates the robust Cl^- diffusion kinetics. Additionally, the morphology variation of the Ni(dpip) electrode after discharge and recharge is given in Fig. 6b and c. Compared to pristine bulk Ni(dpip), the cycled-Ni(dpip) cathode displays the morphology of splitted stacked layers owing to the reversible insertion/deinsertion of a large amount of chloride ions.

Fig. 5 (a) Calculated diffusion pathways of Cl^- in the Ni(dpip) side tubular channel and (b) the corresponding migration energy barrier; (c) calculated diffusion pathways of Cl^- in the Ni(dpip) central tubular channel and (d) the corresponding migration energy barrier.

Fig. 6 (a) Diffusion coefficients of Cl^- in the Ni(dpip) electrode calculated from the GITT in the whole charge/discharge cycle; SEM images of the Ni(dpip) cathode (b) completely discharged at 1.2 V and (c) fully charged to 3.0 V.

Conclusions

In summary, we demonstrate that Ni(dpip) is promising as a new family of cathode materials in CIB systems. The Ni(dpip) electrode exhibited a reversible capacity retained to be 155 mA h g^{-1} after 500 cycles at 150 mA g^{-1} with an extraordinary low capacity decay of 0.026% per cycle and high rate capability with a discharge capacity of 121.6 mA h g^{-1} at 300 mA g^{-1} which is better than those of previously reported CIBs using organic electrolyte. DFT simulations reveal that such superior Cl$^-$ storage behavior with a much higher chloride ion diffusion coefficient is attributed to the open porous frameworks of double 1D tubular channels with various effective opening sizes to facilitate the diffusion and transportation of both charge carriers and electrolytes. The synergetic redox activity of N^0/N$^+$ and Ni^{2+}/Ni^{3+} in the repeating coordination units participated in the electrochemical cycling which endows Ni(dpip) with high Cl$^-$ ion storage capacity. This work thus establishes MOF materials with tubular channels and high porosity as attractive cathodes for anion-type rechargeable batteries.

Data availability

Information supporting this article has been uploaded as part of the ESI.† Additional data is available from the authors on reasonable request.

Author contributions

Qing Yin: data curation, writing-original draft, writing-review & editing, funding acquisition. Zhihao Song: formal analysis, software. Shuhan Yang: formal analysis. Gang-Ding Wang: formal analysis, investigation. Yanwei Sui: resources. Jiqiu Qi: software. Danyang Zhao: visualization, methodology. Lei Hou: supervision, resources. Yong-Zhi Li: software, writing-review & editing, supervision.

Conflicts of interest

The authors have declared no conflict of interest.

Acknowledgements

Notes and references

1 V. K. Davis, C. M. Bates, K. Omichi, B. M. Savoie, N. Momčilović, Q. Xu, W. J. Wolf, M. A. Webb, K. J. Billings, N. H. Chou, S. Alayoglu, R. K. McKenney, I. M. Darolles, N. G. Nair, A. Hightower, D. Rosenberg, M. Ahmed, C. J. Brooks, T. F. Miller, R. H. Grubbs and S. C. Jones, *Science*, 2018, **362**, 1144–1148.

2 X. Zhao, Z. Zhao-Karger, M. Fichtner and X. Shen, *Angew. Chem., Int. Ed.*, 2020, **59**, 5902–5949.

3 T. Liu, N. Peng, X. Zhang, R. Zheng, M. Xia, J. Zhang, H. Yu, L. Zhang and J. Shu, *Energy Storage Mater.*, 2021, **42**, 42–67.

4 L. Zhang, H. Wang, X. Zhang and Y. Tang, *Adv. Funct. Mater.*, 2021, **31**, 2010958.

5 Q. Liu, Y. Wang, X. Yang, D. Zhou, X. Wang, P. Jaumaux, F. Kang, B. Li, X. Ji and G. Wang, *Chem*, 2021, **7**, 1993–2021.

6 G. Karkera, M. A. Reddy and M. Fichtner, *J. Power Sources*, 2021, **481**, 228877.

7 F. Gschwind, H. Euchner and G. Rodriguez-Garcia, *Eur. J. Inorg. Chem.*, 2017, **2017**, 2784–2799.

8 Z. Xue, Z. Gao and X. Zhao, *Energy Environ. Mater.*, 2022, **5**, 1155–1179.

9 T. Li, M. Li, H. Li and H. Zhao, *iScience*, 2021, **24**, 101976.

10 X. Zhao, S. Ren, B. Michael and M. Fichtner, *J. Power Sources*, 2014, **245**, 706–711.

11 X. Zhao, Z. Zhao-Karger, D. Wang and M. Fichtner, *Angew. Chem., Int. Ed.*, 2013, **52**, 13621–13624.

12 T. Yu, Q. Li, X. Zhao, H. Xia, L. Ma, J. Wang, Y. S. Meng and X. Shen, *ACS Energy Lett.*, 2017, **2**, 2341–2348.

13 P. Gao, M. A. Reddy, X. Mu, D. Thomas, L. Zhang, Z. Zhao-Karger, V. S. K. Clemens, O. Chakravadhanula, R. J. Behm and M. Fichtner, *Angew. Chem., Int. Ed.*, 2016, **55**, 4285–4290.

14 M. Wu, X. Lv, J. Wang, R. Wang, X. Shi, H. Zhang, C. Jin, Y. Wei and R. Lian, *J. Mater. Chem. A*, 2021, **9**, 23169–23177.

15 Q. Yin, D. Rao, G. Zhang, Y. Zhao, J. Han, K. Lin, L. Zheng, J. Zhang, J. Zhou and M. Wei, *Adv. Funct. Mater.*, 2019, **29**, 1900983.

16 Q. Yin, J. Luo, J. Zhang, S. Zhang, J. Han, Y. Lin, J. Zhou, L. Zheng and M. Wei, *Adv. Funct. Mater.*, 2020, **30**, 1907448.

17 J. Luo, Q. Yin, J. Zhang, S. Zhang, L. Zheng and J. Han, *ACS Appl. Energy Mater.*, 2020, **3**, 4559–4568.

18 J. Yu, Q. Wang, D. O'Hare and L. Sun, *Chem. Soc. Rev.*, 2017, **46**, 5950–5974.

19 Y. Xu, L. Ma, P. Zhang, Y. Tang, L. Liu, Y. Liu, H. Ding, J. Sun, M. Wang, Z. Li, H.-L. Jiang and W. Chen, *Joule*, 2023, **7**, 515–528.

20 G.-D. Wang, R. Krishna, Y.-Z. Li, W.-J. Shi, L. Hou, Y.-Y. Wang and Z. Zhu, *Angew. Chem., Int. Ed.*, 2022, **61**, e202213015.

21 W. Kang, X. Han, X. Wang, Z. Zhu, B. Zhang, Z. Wang, Y. Wang and D. Sun, *J. Mater. Chem. A*, 2022, **10**, 18185–18194.

22 G.-D. Wang, Y.-Z. Li, W.-J. Shi, L. Hou, Y.-Y. Wang and Z. Zhu, *Angew. Chem., Int. Ed.*, 2022, **61**, e202205427.

23 Y. Xu, X. Zheng, J. Sun, W. Wang, M. Wang, Y. Yuan, M. Chuai, N. Chen, H. Hu and W. Chen, *Nano Lett.*, 2022, **22**, 3298–3306.

24 Y. Zang, F. Pei, J. Huang, Z. Fu, G. Xu and X. Fang, *Adv. Energy Mater.*, 2018, **8**, 1802052.

25 S. Bai, X. Liu, K. Zhu, S. Wu and H. Zhou, *Nat. Energy*, 2016, **1**, 16094.

26 B. Liu, M. Taheri, J. F. Torres, Z. Fusco, T. Lu, Y. Liu, T. Tsuzuki, G. Yu and A. Tricoli, *Nano Lett.*, 2019, **19**, 4391–4399.

27 A. E. Baumann, X. Han, M. M. Butala and V. S. Thoi, *J. Am. Chem. Soc.*, 2019, **141**, 17891–17899.

28 L. Wang, Y. Lu, J. Liu, M. Xu, J. Cheng, D. Zhang and J. B. Goodenough, *Angew. Chem., Int. Ed.*, 2013, **52**, 1964–1967.

29 Y. Tang, W. Li, P. Feng, M. Zhou, K. Wang, Y. Wang, K. Zaghib and K. Jiang, *Adv. Funct. Mater.*, 2020, **30**, 1908754.

30 L. Li, Z. Hu, Y. Lu, C. Wang, Q. Zhang, S. Zhao, J. Peng, K. Zhang, S. Chou and J. Chen, *Angew. Chem., Int. Ed.*, 2021, **60**, 13050–13056.

31 P. Xiao, S. Li, C. Yu, Y. Wang and Y. Xu, *ACS Nano*, 2020, **14**, 10210–10218.

32 J. Xie, X. Li, H. Lai, Z. Zhao, J. Li, W. Zhang, W. Xie, Y. Liu and W. Mai, *Angew. Chem., Int. Ed.*, 2019, **58**, 14740–14747.

33 Y. Li, G. Wang, L. Ma, L. Hou, Y. Wang and Z. Zhu, *ACS Appl. Mater. Interfaces*, 2021, **13**, 4102–4109.

34 Q. Yin, J. Zhang, J. Luo, J. Han, M. Shao and M. Wei, *Chem. Eng. J.*, 2020, **389**, 124376.

35 A. Boucly, F. Rochet, Q. Arnoux, J. Gallet, F. Bournel, H. Tissot, V. Marry, E. Dubois and L. Michot, *Sci. Rep.*, 2018, **8**, 6164.

36 P. Simon, Y. Gogotsi and B. Dunn, *Science*, 2014, **343**, 1210–1211.

37 J. Wang, J. Polleux, J. Lim and B. Dunn, *J. Phys. Chem. C*, 2007, **111**, 14925–14931.

38 Q. Yin, J. Luo, J. Zhang, L. Zheng, G. Cui, J. Han and D. O'Hare, *J. Mater. Chem. A*, 2020, **8**, 12548–12555.

39 G. Zhao, G. Wan, Y. Tang, X. Xu, X. Zhou, M. Zhou, Z. Deng, S. Lin and G. Wang, *Chem. Commun.*, 2020, **56**, 12435–12438.

40 Z. Zhao, T. Yu, Y. Miao and X. Zhao, *Electrochim. Acta*, 2018, **270**, 30–36.

41 X. Zhao, Z. Zhao, M. Yang, H. Xia, T. Yu and X. Shen, *ACS Appl. Mater. Interfaces*, 2017, **9**, 2535–2540.

42 R. Yang, T. Yu and X. Zhao, *J. Alloys Compd.*, 2019, **788**, 407–412.

43 K. P. Lakshmi, K. J. Janas and M. M. Shaijumon, *J. Power Sources*, 2019, **433**, 126685.

44 S. Yang, H. Lv, Y. Wang, X. Guo, L. Zhao, H. Li and C. Zhi, *Angew. Chem., Int. Ed.*, 2022, **61**, e202209794.

45 J. Tabaciarova, M. Micušík, P. Fedorko and M. Omastova, *Polym. Degrad. Stab.*, 2018, **120**, 392–401.